

Cite this: *J. Mater. Chem. A*, 2024, 12, 20056

# Amino acid salt induced $\text{PbI}_2$ crystal orientation optimization for high-efficiency perovskite solar cells with long-term stability†

Jiangying Lu,<sup>a</sup> Yulin Wu,<sup>bc</sup> Shan Wu,<sup>a</sup> Jing Zhao,<sup>bc</sup> Jinyao Wang,<sup>bc</sup> Runkang Lin,<sup>bc</sup> Huayi Zou,<sup>bc</sup> Shudi Lu,<sup>d</sup> Kong Liu,<sup>bc</sup> Shizhong Yue,<sup>bc</sup> Zhijie Wang,<sup>bc</sup> Liya Zhou<sup>\*a</sup> and Shengchun Qu<sup>bc</sup>

The two-step method presents an efficient means to streamline the fabrication process of high-quality and reproducible perovskite films, making it a more suitable option for the fabrication of large-scale commercial perovskite solar cells. However, a challenge with the two-step method lies in the incomplete conversion of  $\text{PbI}_2$ , leading to decreased device performance. To address this issue, potassium L-glutamate (PL-Glu) is introduced to modify the crystal orientation of  $\text{PbI}_2$ , yielding a perovskite buried interface devoid of any  $\text{PbI}_2$  residue. This modification enables better infiltration of FAI, resulting in perovskite films with enhanced crystal quality, thereby significantly reducing the adverse impact of non-radiative recombination caused by the incomplete conversion of  $\text{PbI}_2$ . Moreover, this method optimizes the energy level structure of the  $\text{SnO}_2$  electron transport layer, improving charge transport efficiency at the perovskite/ $\text{SnO}_2$  interface. Consequently, n-i-p perovskite solar cells achieve a power conversion efficiency (PCE) of 24.1% with a high fill factor of 82.9%. The PL-Glu-modified device maintained 92% of the initial PCE after 2700 hours under nitrogen. This study provides a novel engineering strategy for simultaneously optimizing perovskite absorbers and interfaces.

Received 3rd April 2024  
Accepted 9th June 2024

DOI: 10.1039/d4ta02248c

rsc.li/materials-a

## Introduction

Perovskite solar cells (PSCs), owing to their advantages including low exciton binding energy, high defect tolerance,

excellent absorption efficiency, and tunable band gap, have garnered significant attention as a promising next-generation photovoltaic technology.<sup>1–6</sup> The power conversion efficiency (PCE) of single-junction perovskite solar cells has witnessed a remarkable enhancement, reaching 26.1%, on par with the traditional silicon solar cells.<sup>7</sup> Notably, the fabrication of highly efficient and stable perovskite thin films has predominantly relied on a one-step antisolvent deposition method. However, this approach is constrained by a narrow processing window and an uncontrollable crystallization rate, potentially leading to small perovskite grain sizes and uneven surface coverage. Furthermore, the reproducibility of device performance is compromised compared to the two-step method. Meanwhile, the commonly used antisolvents, such as toluene and chlorobenzene, are highly toxic.<sup>8–10</sup> These challenges pose significant hurdles in the industrialization of PSCs.

An alternative approach to perovskite preparation involves the two-step sequential deposition technique, offering a broader processing window and obviating the need for antisolvents.<sup>11,12</sup> In this method, the formation of perovskite film



Shizhong Yue

Shizhong Yue received his PhD degree from the Institute of Semiconductors, Chinese Academy of Sciences (CAS), in 2018. From 2018 to 2022, he joined the Materials and Science of Engineering, at the National University of Singapore, as a research fellow. In 2022, he moved to the Institute of Semiconductors, CAS as a professor. His current research interests focus on perovskite solar cells, thermoelectric materials and related energy areas.

<sup>a</sup>Department School of Chemistry and Chemical Engineering, Guangxi University, Nanning 530004, China. E-mail: zhouliya@gxu.edu.cn

<sup>b</sup>Key Laboratory of Semiconductor Materials Science and Beijing Key Laboratory of Low Dimensional Semiconductor Materials and Devices, Institute of Semiconductors, Chinese Academy of Sciences, Beijing, 100083, China. E-mail: yueshizhong@semi.ac.cn; qsc@semi.ac.cn

<sup>c</sup>Center of Materials Science and Optoelectronics Engineering, University of Chinese Academy of Sciences, Beijing 100049, China

<sup>d</sup>Department of Physics, Hebei Normal University of Science & Technology, Qinhuangdao 066004, China

† Electronic supplementary information (ESI) available. See DOI: <https://doi.org/10.1039/d4ta02248c>

depends on molecular exchange, wherein the second-step reaction typically involves multiple organic components, presenting difficulties in accurately regulating the chemical composition of the film. Another common issue in this process is incomplete conversion of  $\text{PbI}_2$ , where the pre-deposited  $\text{PbI}_2$  tends to form dense, less reactive crystals. This impedes the diffusion of large ions  $\text{FA}^+$  into the  $\text{PbI}_2$  interior and their insertion into the  $[\text{PbI}_6]_4$  framework. Consequently, disordered perovskite growth and residual  $\text{PbI}_2$  inevitably lead to reduced device performance.<sup>11,13</sup> To address this issue, various methods and strategies have been developed, including the utilization of solvents with different polarities,<sup>14</sup> medication of the perovskite crystallization process,<sup>15</sup> and the creation of loose, porous  $\text{PbI}_2$  structures.<sup>16,17</sup> For instance, Sun *et al.* produced porous and fluffy lead iodide layers by adding quaternary ammonium halide (QAH) additives into  $\text{PbI}_2$ .<sup>18</sup> However, the reaction at the buried interface of the perovskite has not been studied. Shao *et al.* modulated nucleation and crystallization of the  $\text{PbI}_2$  films by introducing PFAT into  $\text{PbI}_2$  precursor solutions and obtained preferentially oriented perovskite films with a largely reduced residual  $\text{PbI}_2$  content.<sup>15</sup> However, the PCE champion of the device modified only by PFAT is 23.13%, which is slightly insufficient in terms of device efficiency. Therefore, it is important and necessary to investigate how interface modification affects the crystallization of  $\text{PbI}_2$  and the crystalline quality of perovskite.

In this study, we reported the utilization of potassium L-glutamate (PL-Glu) to modulate the crystallographic orientation of  $\text{PbI}_2$  for sequential deposition of black-phase FAPbI<sub>3</sub>, aiming at highly efficient and stable PSCs. We observed that PL-Glu induced the dispersion and refinement of  $\text{PbI}_2$  grains in the buried layer, with crystal grains in the upper layer tended to grow along the (001) crystal plane. As the grains enlarged, gaps increased, which facilitated the penetration of the FAI and resulted in a perovskite film without residual  $\text{PbI}_2$  at the buried interface. Moreover, the integration of PL-Glu modified the energy level structure of the  $\text{SnO}_2$  electron transport layer (ETL) and enhanced the charge transfer between the perovskite buried interface and the  $\text{SnO}_2$ . These modifications facilitated the suppression of non-radiative carrier recombination and acceleration of electron extraction between perovskite and  $\text{SnO}_2$ . As a result, the PSCs with PL-Glu modification achieved a PCE up to 24.1%, with a high fill factor (FF) of 82.9%, representing a noteworthy advancement compared with the unmodified device, which had a PCE of only 22.66% and FF of 80.6%.

## Results and discussion

### Crystallization of $\text{PbI}_2$ and its effect on the morphology of the perovskite buried interface

During the two-step process of preparing perovskite films, a dense  $\text{PbI}_2$  film can be easily obtained in the first step. However, it can be challenging for the FAI deposited in the second step to diffuse into the buried of the  $\text{PbI}_2$  film and induced a complete reaction.<sup>19</sup> Previous studies have indicated that a significant amount of unreacted  $\text{PbI}_2$  remains at the

buried interface of perovskite.<sup>20,21</sup> We found that using potassium L-glutamate (PL-Glu) as an interface treatment material on  $\text{SnO}_2$  can regulate the crystallization of  $\text{PbI}_2$  at the buried interface, resulting in an improvement in the incomplete reaction of  $\text{PbI}_2$  at the buried interface of perovskites.

To directly analyze the components of the interface without destroying its structure, we developed two testing methods utilizing Grazing Incidence X-ray diffraction (GIXRD), X-ray incident from the back side (Fig. 1a) and peeling off method (Fig. 1c). Consistent with results in published works, unreacted  $\text{PbI}_2$  is identifiable at the buried interface of perovskite. As illustrated in Fig. 1b, a distinct peak of the  $\text{PbI}_2$  (001) crystal plane was observed at  $12.9^\circ$ . Similar results were obtained in the peeling-off method (Fig. 1d). In particular, compared to the control perovskite ( $\text{SnO}_2$  layers without PL-Glu treatment), the perovskite film deposited on PL-Glu- $\text{SnO}_2$  exhibited no characteristic peak of  $\text{PbI}_2$ , and only the (100) crystal plane characteristic peak of FAPbI<sub>3</sub> was observed (Fig. 1d). In order to elucidate the underlying causes for this change,  $\text{PbI}_2$  with varying concentrations was coated on control  $\text{SnO}_2$  and PL-Glu modified  $\text{SnO}_2$ , producing  $\text{PbI}_2$  layers of distinct thicknesses. Wide-Angle X-ray Diffraction (XRD) patterns were employed to investigate the crystallization of  $\text{PbI}_2$  layers before and after modification. At a  $\text{PbI}_2$  concentration of 0.065 M (Fig. 1e), the characteristic peak of  $\text{PbI}_2$  at  $12.8^\circ$  was observed before and after modification. In the enlarged figure, it was noted that the characteristic peak of  $\text{PbI}_2$  shifted to a large angle after modification, and the peak shape broadened, indicating that PL-Glu modification induces a shrinkage in the underlying  $\text{PbI}_2$  unit cell, resulting in a reduction in the lattice constant and the crystal grains. The full width at half maxima (FWHM) of the  $\text{PbI}_2$  (001) crystal plane was calculated using the Debye-Scherrer formula. It was found to be 0.91 before modification and increased to 0.95 after modification (Fig. S1†). At a  $\text{PbI}_2$  concentration of 0.13 M, there was a noticeable change in the variation trend of the characteristic peak of the (001) crystal plane of  $\text{PbI}_2$ . The intensity of the (001) crystal plane characteristic peak of the PL-Glu modified sample was significantly enhanced and sharper compared to that of the control  $\text{SnO}_2$  sample. This indicates that the PL-Glu modification enhances the orientation of  $\text{PbI}_2$  in the upper layer (relative to the underlying) in the (001) crystal plane. The full width at half maxima (FWHM) of the  $\text{PbI}_2$  (001) crystal plane was calculated using the Debye-Scherrer formula. It was found to be 0.471 before modification and increased to 0.456 after modification (Fig. S2†), indicating that the  $\text{PbI}_2$  grains were enlarged after modification leading to larger grains. This phenomenon is also observable through SEM images (Fig. S3†).

Moreover, upon comparing the film cross-sections of 0.13 M  $\text{PbI}_2$  on  $\text{SnO}_2$  before and after modification, no significant changes in the thickness of  $\text{PbI}_2$  were observed (Fig. S4†). As the (001) crystal plane dominates the crystal,  $\text{PbI}_2$  forms a plate-like morphology with larger grains. Consequently, the gaps between these grains are also larger than those in small grains, providing channels for the subsequent penetration of FAI.<sup>22</sup> As shown in Fig. S5,†  $\text{PbI}_2$  films upon the PL-Glu- $\text{SnO}_2$  displays a reduced arithmetic mean roughness ( $R_a$ ) value on the surface roughness

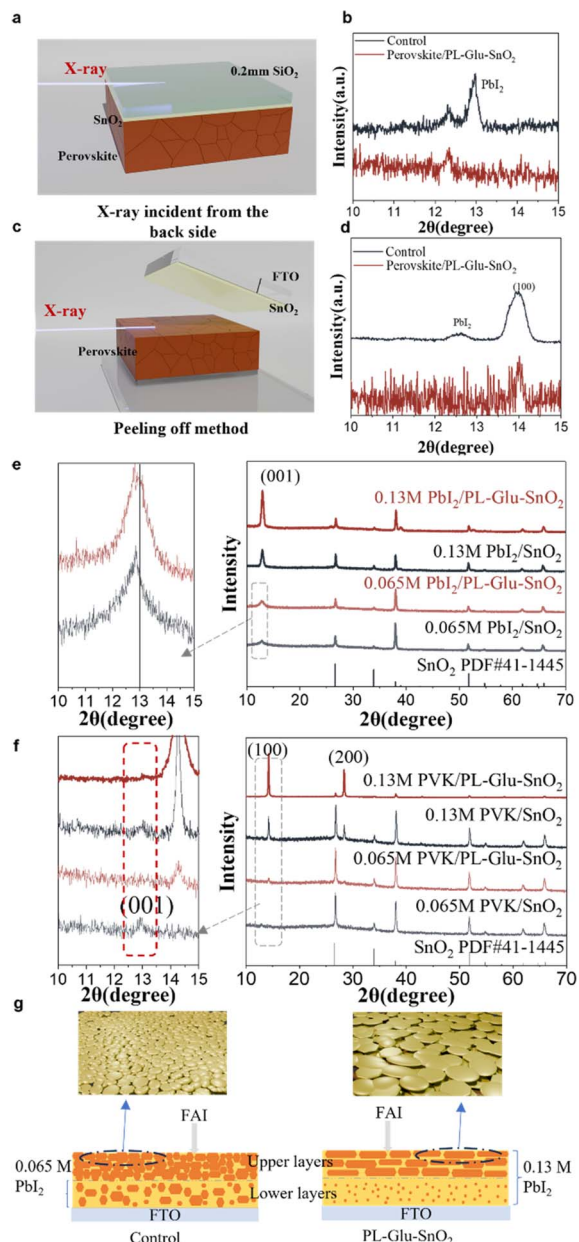


**Fig. 1** (a) Schematic of the X-ray incident from the back side. (b) GIXRD patterns of perovskite film substrate at an incidence angle of  $1^\circ$ , incident from a quartz surface. (c) Schematic of the peeling off method. (d) GIXRD patterns of the buried surface of the perovskite film at an incidence angle of  $0.1^\circ$ . (e) XRD patterns of 0.065 M and 0.13 M  $\text{PbI}_2$ . (f) XRD patterns of 0.065 M and 0.13 M perovskite. (g) Schematic diagram of  $\text{PbI}_2$  crystallization before and after PL-Glu modification.

of 5.73 nm compared to that of control  $\text{SnO}_2$  (6.39 nm). The statement above suggests that the introduction of PL-Glu leads to an increase in the size of  $\text{PbI}_2$  grains and the pores between them. These changes are expected to facilitate the penetration of organic ammonium salts and the volatilization of solvents during the annealing process.

To investigate the impact of PL-Glu on the crystallinity of the buried interface perovskite layer, we reacted the aforementioned concentration of  $\text{PbI}_2$  with an equal proportion of

organic ammonium to form perovskite. This method can be used to investigate the reaction between FAI and  $\text{PbI}_2$  at various depths before and after PL-Glu modification, aiding in the exploration of how PL-Glu enhances the bottom interface of perovskite. Fig. 1f displays the XRD results, while Fig. 1g provides a schematic diagram. When  $\text{PbI}_2$  concentration is 0.065 M, only characteristic peak of the (001) crystal plane of  $\text{PbI}_2$  is observed on the control  $\text{SnO}_2$  in the magnified figure. However, the PL-Glu modified  $\text{SnO}_2$  shows the characteristic peak of the (110) crystal plane of  $\text{FAPbI}_3$ , with no discernible characteristic peak of  $\text{PbI}_2$ . Upon increasing the concentration to 0.13 M, the (110) crystal plane of perovskite becomes evident both before and after modification. Nevertheless, the characteristic peak of the (001) crystal plane of  $\text{PbI}_2$  is still present on the control  $\text{SnO}_2$  sample. This indicates that the introduction of PL-Glu alters the crystallization of  $\text{PbI}_2$  and promotes the complete conversion of  $\text{PbI}_2$  at the buried interface to generate  $\text{FAPbI}_3$ .

After contact with the FAI, the  $\text{PbI}_2$  cluster with suitable size undergoes secondary nucleation, forming larger clusters. Larger clusters subsequently interact with the FAI to generate perovskite, while smaller clusters below the critical size are depleted, enabling the growth of larger clusters.<sup>23</sup> During the interaction between FAI and  $\text{PbI}_2$ ,  $\text{PbI}_2$  exceeding the critical cluster size in the upper layer transforms into perovskite. Meanwhile, a small amount of FAI penetrates into the bottom interface, reacting with the remaining lower layers of  $\text{PbI}_2$  grains. In this process, the lower layers of  $\text{PbI}_2$  of the PL-Glu modified sample were consumed by the upper  $\text{PbI}_2$  due to secondary crystallization, and the remaining fully reacted with FAI. In contrast, the control group exhibits larger  $\text{PbI}_2$  cluster sizes in the lower layers, with less FAI penetrating into these layers for interaction with  $\text{PbI}_2$ , causing an increase in residual  $\text{PbI}_2$ .

In the two-step method, the deposited  $\text{PbI}_2$  undergoes further crystallization, followed by FAI intercalation and the formation of the perovskite phase. Previous studies have demonstrated through theoretical calculations that the (001) crystal plane is the optimal orientation for perovskite films.<sup>24,25</sup> Therefore, increasing the crystallinity of the (001) crystal face of  $\text{PbI}_2$  by PL-Glu modification helps to obtain high-quality perovskite films. We then performed scanning electron microscopy (SEM) to visualize and analyze the effects of PL-Glu on the buried perovskite interfaces. Fig. 2a illustrates the process of peeling the perovskite film (details in the ESI†). The Energy Dispersive Spectrometer (EDS) results (Fig. S6†) of  $\text{SnO}_2$  after perovskite exfoliation show no residual perovskite components on the surface, indicating a complete perovskite buried interface can be achieved through the exfoliation method. Fig. 2b and c show that a significant amount of white granular material is present at the perovskite buried interface of the control sample, continuously distributed at the grain boundaries of the perovskite. This material has been confirmed to be  $\text{PbI}_2$  through EDS analysis (Fig. 2f and g). Incomplete reaction of  $\text{PbI}_2$  is due to the hindered diffusion of FAI. At the buried interface of the perovskite deposited on PL-Glu- $\text{SnO}_2$  (Fig. 2d and e), there is no visible white substance in the gaps between the grains. The perovskite grains are larger and

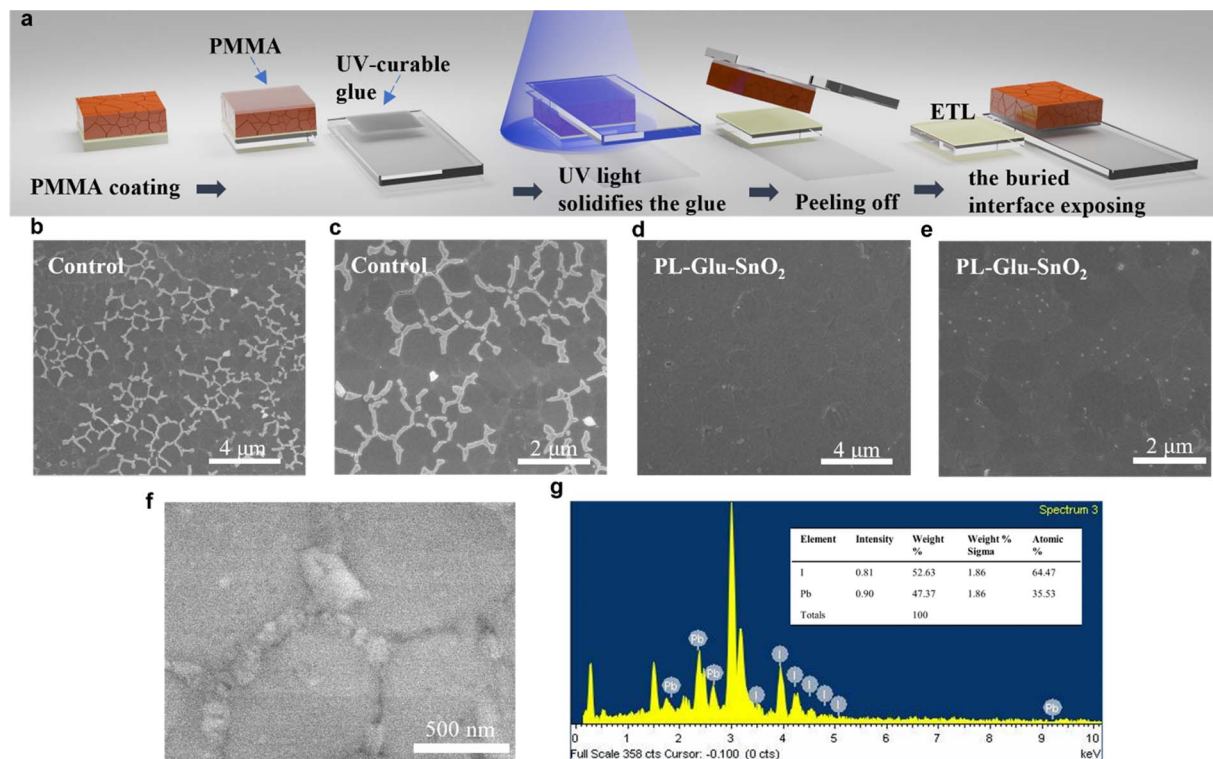


Fig. 2 (a) Schematic of the peel-off process. (b–e) The morphologies for buried interface of the perovskite films deposited on the Control SnO<sub>2</sub> (b, and c) and the PL-Glu-SnO<sub>2</sub> (d, and e). (f) SEM image corresponding to the EDS characterization of the white material between grains of perovskite buried interface. (g) EDS result of the white substance between grains of perovskite buried interface.

smoother compared to the control. The incomplete reaction of PbI<sub>2</sub> at the perovskite buried interface is improved by the introduction of PL-Glu. The SEM observations are consistent with our XRD analysis results.

The morphology and crystallographic orientation of the PbI<sub>2</sub> film during the continuous film deposition process significantly affect the quality of the resulting perovskite film. In order to provide the strategies for adjusting the crystallization of PbI<sub>2</sub>, SEM was used to characterize the difference in perovskite morphology before and after treatment with PL-Glu. In comparison to the control device, the sample treated with PL-Glu presents a smoother and denser film, with a notable reduction in unreacted PbI<sub>2</sub> on the upper surface (Fig. 3a and c). When analyzing the perovskite cross-section, the PL-Glu-treated sample exhibits fewer perovskite grain boundaries and significantly larger grain sizes than the control device (Fig. 3b and d). This improves the vertical charge transport within the device. Moreover, PL-Glu modification reduced the  $R_a$  of the perovskite film from 19.1 nm to 17.9 nm (Fig. 3e and f). This flat and uniform morphology with low surface roughness is critical for suppressing charge defects and reducing interfacial series resistance for efficient charge transport.<sup>26</sup> The influence on the crystalline and absorptive properties of the perovskite films were characterized by UV-vis absorption spectra and XRD. In Fig. 3g, the film exhibits diffraction peaks at 14.3° and 28.5°, corresponding to (100) and (200) crystal planes of FAPbI<sub>3</sub>.<sup>27,28</sup> The intensities of the main diffraction peaks of perovskite

increase upon PL-Glu modification, indicating an enhancement in the crystallinity of the perovskite. Additionally, the Ultraviolet-visible (UV-vis) absorbance (Fig. S7†) demonstrates an increase after modification, which contributes to the increase in current density.

The adsorption energy of FA<sup>+</sup> cations on the PbI<sub>2</sub> (001) crystal plane is greater than that on the (110) crystal plane. This suggests that the (001) crystal plane is more likely to react with FA<sup>+</sup> cations to form perovskite.<sup>29</sup> The PL-Glu modification enhances the crystallinity of the PbI<sub>2</sub> (001) crystal plane, facilitating the formation of larger PbI<sub>2</sub> grains. This is conducive to the reaction with FA<sup>+</sup> to form perovskite. Consequently, the crystallinity of the perovskite prepared following PL-Glu modification is demonstrably superior to that of the control sample. The PL-Glu modification has a synergistic effect on the bottom and surface of the perovskite and the grain size of the bottom interface of the perovskite. The crystallization of the upper interface of the perovskite is reduced, and the roughness is reduced, which is conducive to the carrier transport and extraction between the perovskite and the ETL and HTL.<sup>30</sup>

#### Effect of buried interface modification on SnO<sub>2</sub> performance

SnO<sub>2</sub> possesses a large number of defects on its upper surface. These defects originate from surface atoms with inadequate coordination and may induce energetically deep gap states.<sup>31,32</sup> When interfaced with perovskites, the states in SnO<sub>2</sub> can both increase charge carrier recombination and hinder the collection

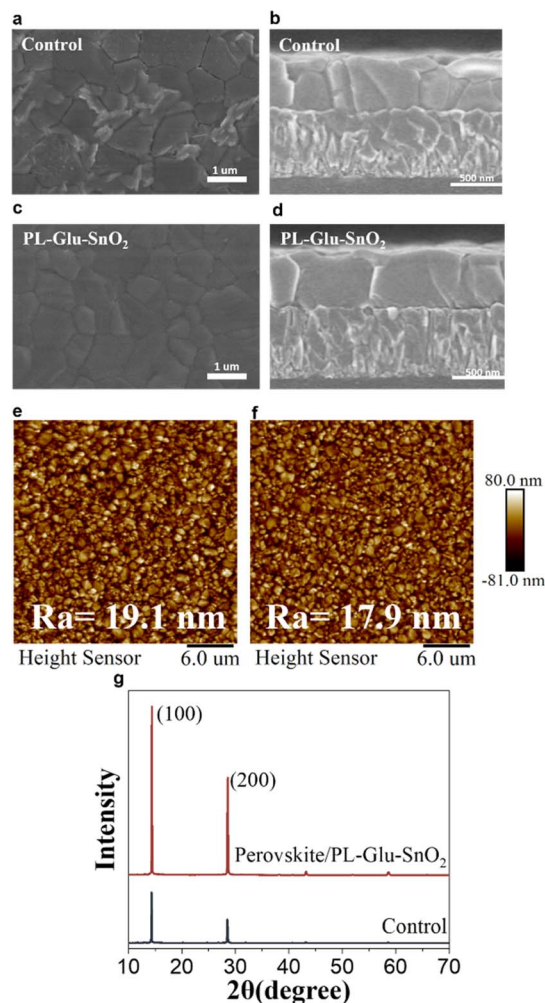


Fig. 3 (a) Top-view SEM and (b) cross-sectional SEM images of perovskite films deposited on the control SnO<sub>2</sub>. (c) Top-view SEM and (d) cross-sectional SEM images of perovskite films deposited on the PL-Glu-SnO<sub>2</sub> coated FTO substrates. (e) AFM images of perovskite films deposited on the control SnO<sub>2</sub> and (f) the PL-Glu-SnO<sub>2</sub>. (g) XRD patterns of perovskite film.

and transfer of free charges carriers that ultimately reduce device performance.<sup>33</sup> Therefore, an ideal contact surface modification material should not only solve the problem of incomplete reaction of PbI<sub>2</sub> at the buried interface of perovskite but also regulate the energy level and passivate defects on the upper surface of SnO<sub>2</sub>.

Calculations based on density functional theory (DFT) were carried out to map out the electrostatic potential (ESP), which visualizes the charge distribution of the PL-Glu molecule. The chemical structure and the ESP map of PL-Glu zwitterion are shown in Fig. S8† and 4a, respectively. It is evident from the color gradient that there is a gradual decrease in electron density from the negative center (–COO<sup>–</sup> group) to the positive center (–NH<sup>2+</sup> group and carbon skeleton) in the structure. Potassium glutamate's carboxylic acid is expected to interact with SnO<sub>2</sub>, while the amino group undergoes an acid–base coordination reaction with PbI<sub>2</sub>.

To explore the impact of PL-Glu on the chemical environment of the SnO<sub>2</sub> layer, we initially investigated the interactions between SnO<sub>2</sub> and PL-Glu *via* the X-ray photoelectron spectroscopy (XPS) technique. As illustrated in Fig. 4b, the significant N 1s signals confirm the existence of PL-Glu on the surface of SnO<sub>2</sub>. Additionally, the SnO<sub>2</sub> film modified with PL-Glu displayed shifted Sn 3d peaks (Fig. 4c), from 495.14 eV and 486.73 eV to 495.23 eV and 486.83 eV, respectively. This change in electron density can be attributed to the negative charge carried by –COO<sup>–</sup>.<sup>34</sup> The O 1s signals of the control SnO<sub>2</sub> films displayed two separate peaks in Fig. 4d: one corresponding to lattice oxygen (530.66 eV), and the other depicting chemisorbed oxygen atoms or hydroxyl groups (531.86 eV).<sup>35</sup> After the modification with PL-Glu, the intensity of the peak representing lattice oxygen decreased, while that for adsorbed oxygen increased. The shifting Sn 3d and O 1s peaks suggest a chemical interaction between PL-Glu and SnO<sub>2</sub>. These observations suggest a chemical interaction between PL-Glu and SnO<sub>2</sub>. Such interaction arises from the coordination between the carboxyl groups and under-coordinated Sn<sup>4+</sup>.<sup>32,34</sup> Furthermore, Fourier-transform infrared spectroscopy (FTIR) measurement (Fig. S9†) was performed to analyze the interaction of PL-Glu with the SnO<sub>2</sub> layer. The FTIR spectrum of PL-Glu shows a typical –COO<sup>–</sup> stretching vibration at ≈ 1600 cm<sup>–1</sup>. Following the modification of PL-Glu on SnO<sub>2</sub>, a blue shift in the –COO<sup>–</sup> stretching vibration peak was observed, indicating the interaction between SnO<sub>2</sub> and –COO<sup>–</sup> on PL-Glu.<sup>36</sup> This finding agrees with the XPS analysis results.

Since PL-Glu interacts with both the SnO<sub>2</sub> and the perovskite buried interface, the energy levels of the SnO<sub>2</sub> film and the perovskite buried interface may change due to PL-Glu modification, thus potentially impacting the charge transfer at the perovskite buried interface. The  $E_{\text{VB}}$  and  $E_{\text{CB}}$  of perovskite, the control SnO<sub>2</sub>, and PL-Glu-SnO<sub>2</sub> were obtained through UPS and UV-vis testing (Fig. S10†). Fig. 4g illustrates the energy level alignment. The  $E_{\text{CB}}$  (–3.72 eV) of SnO<sub>2</sub> is slightly upshifted after PL-Glu modification and is closer to that of perovskite (–3.56 eV) compared with SnO<sub>2</sub> (–3.83 eV). This can reduce the loss of open circuit voltage ( $V_{\text{oc}}$ ), which helps to improve the final PCE of the device.

### Photovoltaic performance of the PSCs

To further analyze the carrier dynamics of perovskite films grown on SnO<sub>2</sub> before and after modification, we performed a series of optical and electrical characterizations. Fig. 5a and S11† shows the steady-state photoluminescence of the perovskite film before and after modification. Compared to the control SnO<sub>2</sub>, the perovskite film on PL-Glu modified SnO<sub>2</sub> shows lower PL intensity at a wavelength of 802 nm, indicating that the PL-Glu modification results in more efficient electron injection. Additionally, time-resolved photoluminescence (TRPL) measurements were also performed on the same sample, and the PL intensity decay curves plotted in Fig. 4b were fitted with a bi-exponential decay equation:

$$I(t) = I_0 + A_1 e^{-t/\tau_1} + A_2 e^{-t/\tau_2}$$

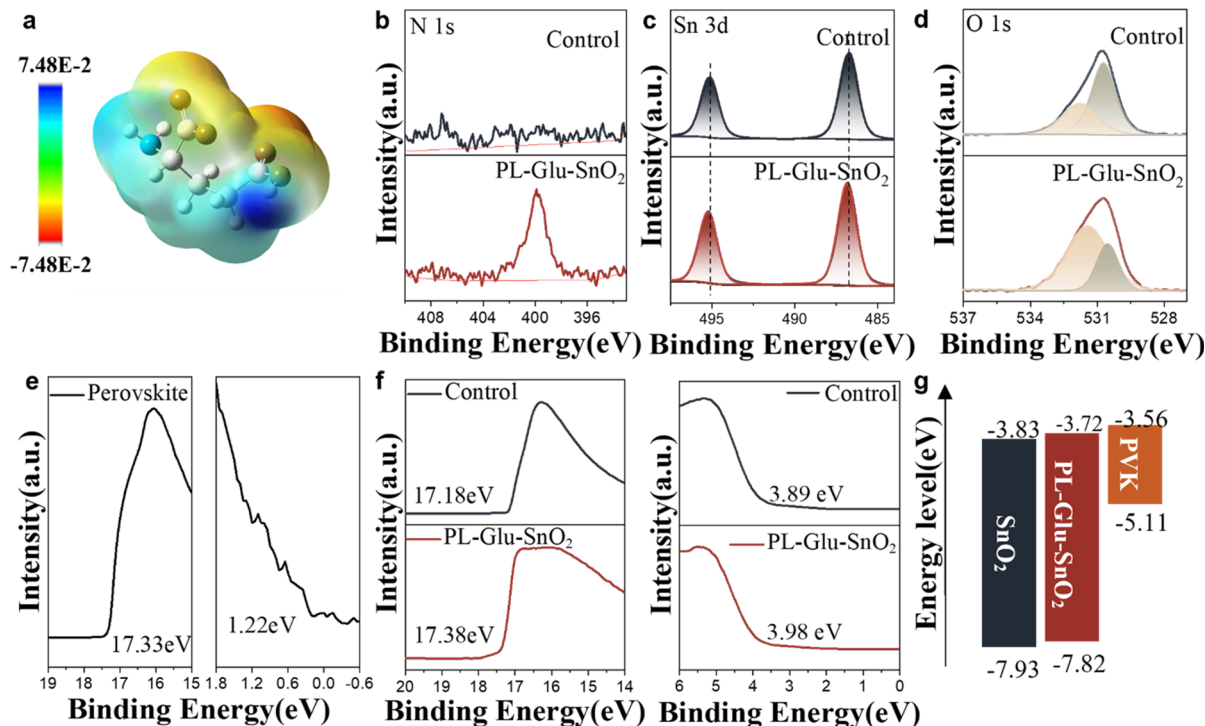


Fig. 4 (a) ESP map of L-Glu anion. The XPS of N 1s (b), Sn 3d (c) and O 1s (d) of  $\text{SnO}_2$  with or without the PL-Glu modification. (e) UPS spectra of perovskite films. (f) UPS spectra of the control  $\text{SnO}_2$  and PL-Glu- $\text{SnO}_2$  films. (g) Energy level diagram of ETL and perovskite (vs. vacuum energy level).

TRPL spectra show that the charge carrier lifetime after PL-Glu modification is shorter (45.3 ns) compared to the control perovskite film (301.6 ns). The shorter lifetime indicates that the electron extraction efficiency at the  $\text{SnO}_2$  ETL/perovskite

interface is higher after PL-Glu modification.<sup>37</sup> Fig. S12<sup>†</sup> displays the TRPL results following modification with varying concentrations of PL-Glu (0.01–0.03 M).

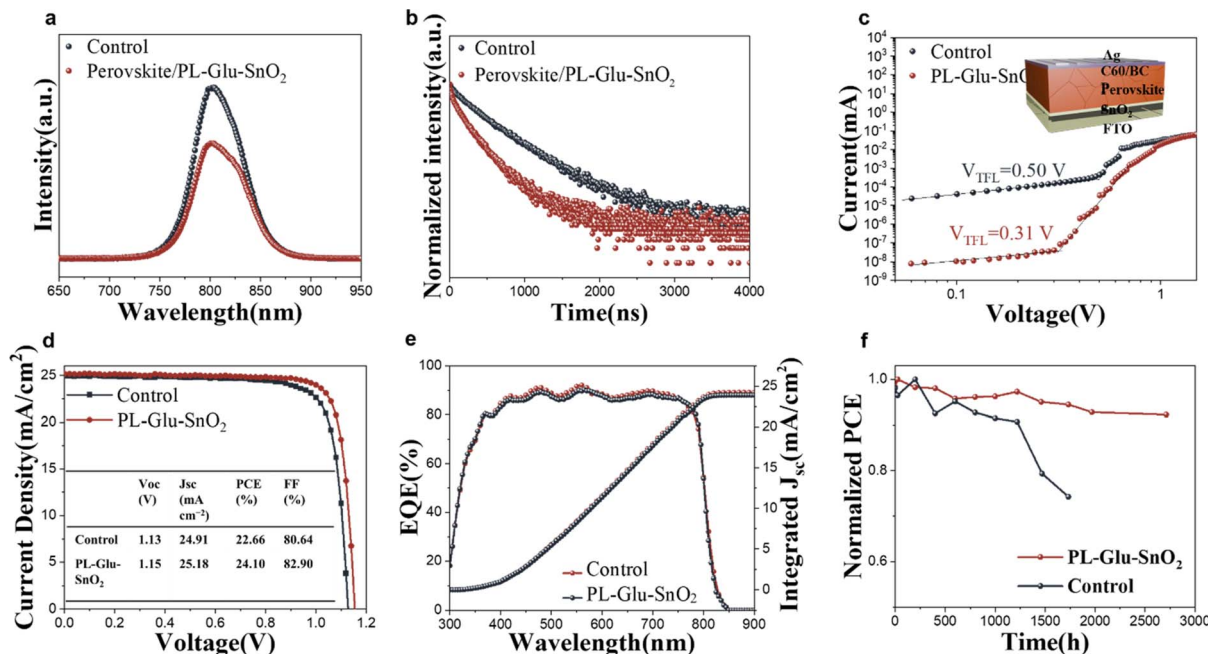


Fig. 5 (a) Steady-state PL of  $\text{SnO}_2$ /perovskite film and PL-Glu- $\text{SnO}_2$ /perovskite film. (b) TRPL curves of  $\text{SnO}_2$ /perovskite film and PL-Glu- $\text{SnO}_2$ /perovskite film. (c) Dark  $J$ - $V$  measurement of control and PL-Glu- $\text{SnO}_2$ /perovskite electron-only devices. Inset: schematic illustration of the device structure. (d)  $J$ - $V$  curves of target and control PSCs. (e) EQE spectra and the corresponding integrated  $J_{sc}$  of the target and control PSCs. (f) Storage stability of the unencapsulated target and control PSC at room temperature in the dark in glovebox.

To further quantitatively study the effect of PL-Glu modification on the defect density of perovskite, electron-only devices with FTO/SnO<sub>2</sub>/(W/O or W PL-Glu)/perovskite/C60/BCP/Ag structure were prepared and measured by the space charge current limiting (SCLC) method.<sup>38</sup> The trap-filled limit voltage ( $V_{\text{TFL}}$ ) of the control device and the PL-Glu modified single electron device are 0.54 and 0.31 V, respectively (Fig. 5c). Based on these results, it is calculated that the electron defect density of the PL-Glu modified device is  $5.03 \times 10^{15} \text{ cm}^{-3}$ , which is lower than the control film ( $9.78 \times 10^{15} \text{ cm}^{-3}$ ). Reducing the density of defects is beneficial in suppressing non-radiative recombination, thereby improving device performance.

At last, we fabricated solar cells with an n-i-p structure of FTO glass/SnO<sub>2</sub>/perovskite/Spiro-OMeTAD/Ag. After optimization of the PL-Glu concentration (0.01–0.03 M) in solar cells (Fig. S13<sup>†</sup>), an optimal ratio of PL-Glu (0.02 M) in SnO<sub>2</sub> led to a champion efficiency of 24.10% (Fig. 5e), with open-circuit voltage ( $V_{\text{oc}}$ ) of 1.15 V, short-circuit current density ( $J_{\text{sc}}$ ) of 25.18 mA cm<sup>-2</sup> and a fill factor (FF) of 82.9%. While for the control devices, the PCE of the champion device was 22.66%, and the corresponding  $J_{\text{sc}}$ ,  $V_{\text{oc}}$ , and FF were 24.91 mA cm<sup>-2</sup>, 1.13 V, and 80.6%, respectively. The hysteresis index (HI), calculated by the formula  $\text{HI} = (\text{PCE}_{\text{RS}} - \text{PCE}_{\text{FS}})/\text{PCE}_{\text{RS}}$ , exhibits a pronounced decline from 4.0% to 1.6% (Fig. S14<sup>†</sup>). This decline can be attributed to the efficient carrier transport at the PL-Glu modified SnO<sub>2</sub>/perovskite interface. Increasing the PL-Glu concentration above 0.02 M results in a decrease in FF, possibly because the high loading of insulating PL-Glu increases the internal series resistance, preventing efficient charge transfer at the interface. The EQE (external quantum efficiency) results (Fig. 5d) revealed that the integrated  $J_{\text{sc}}$  of the device before and after optimization of the PL-Glu was 23.90 and 24.23 mA cm<sup>-2</sup>, respectively, which well matched with the  $J_{\text{sc}}$  value obtained by  $J$ - $V$  curves in Fig. 5e.

Long-term stability is a crucial quality assurance for PSCs to advance towards commercialization. Hence, we performed stability tests on PSCs with and without PL-Glu modification. The testing apparatus was kept under nitrogen conditions and the results are presented in Fig. 5f. It is clear from the results that the device with PL-Glu modification exhibits superior stability. Specifically, the PCE of this device remains above 92% of its initial PCE even after storage for 2700 hours. The control device's PCE decreased significantly after 1200 hours, dropping to 75% by 1700 hours. To ascertain the stability under working conditions of the devices, we conducted a test on the steady-state photocurrent output of PSCs at the maximum power point (MPP) following 150 seconds of illumination (Fig. S15<sup>†</sup>). For PL-Glu-SnO<sub>2</sub> devices, steady-state efficiencies were remained at 23.94% under bias voltages of 0.988 V. In contrast, control exhibited a decreasing trend, from 22.48% to 21.90% under bias voltages of 0.968 V. This suggests that the working stabilization of the PL-Glu modified device has been enhanced.

## Conclusions

Through the application of the molecular modifier PL-Glu to the buried interface between SnO<sub>2</sub> and the perovskite layer,

enhancement in both the efficiency and stability of perovskite solar cells can be achieved simultaneously. Systematic analysis showed that PL-Glu can change the crystal orientation and crystallinity of PbI<sub>2</sub>, improve the incomplete reaction of PbI<sub>2</sub>, and optimize crystal growth on the perovskite surface. Moreover, PL-Glu can interact with the suspended bond on the SnO<sub>2</sub> surface to adjust the energy level of the perovskite layer, thereby promoting interfacial charge transfer. The enhanced film quality possesses lower defect density, which is essential for reducing non-radiative charge recombination and prolonging charge lifetime. Consequently, FAPbI<sub>3</sub>-based PSCs with PL-Glu modification demonstrate significant improvement of  $V_{\text{oc}}$  and FF, leading to PCE increased to 24.10% under 100 mA cm<sup>-2</sup> illumination, higher than the control devices (22.66%). Meanwhile, the PL-Glu-modified device maintained 92% of the initial PCE after 2700 hours under nitrogen, whereas the control device merely retained 75% of its initial efficiency after 1200 hours. The PL-Glu-modified strategy provides a new way to improve the PCE and stability of two-step perovskite solar cells.

## Data availability

The data that support the findings of this study are available on request from the corresponding author, upon reasonable request.

## Author contributions

J. L. conceived the idea and designed the experiments. J. L. and Y. W. fabricated the devices and conducted the characterization. All authors participated in data analysis and discussion. S. Y. and L. Z. supervised the project. J. L. wrote the paper. All authors reviewed the paper.

## Conflicts of interest

There are no conflicts to declare.

## Acknowledgements

This work was mostly supported by the National Natural Science Foundation of China (Contract No. U20A20206, 51972300, 62274155, and 62304219), the Strategic Priority Research Program of the Chinese Academy of Sciences (Grant No. XDB43000000), CAS Project for Young Scientists in Basic Research (YSBR-090), and the National Key Research and Development Program of China (Grant No. 2023YFB3611200). Professor K. L. appreciates the support from the Youth Innovation Promotion Association, Chinese Academy of Sciences (No. 2020114).

## Notes and references

- 1 T. L. Bu, J. Li, H. Y. Li, C. C. Tian, J. Su, G. Q. Tong, L. K. Ono, C. Wang, Z. P. Lin, N. Y. Chai, X.-L. Zhang, J. J. Chang, J. F. Lu, J. Zhong, W. C. Huang, Y. B. Qi, Y.-B. Cheng and F. Z. Huang, *Science*, 2021, **372**, 1327–1332.

- 2 S. Sánchez, S. Cacovich, G. Vidon, J.-F. Guillemoles, F. Eickemeyer, S. M. Zakeeruddin, J. E. K. Schawe, J. F. Löffler, C. Cayron, P. Schouwink and M. Graetzel, *Energy Environ. Sci.*, 2022, **15**, 3862–3876.
- 3 J. J. Xue, R. Wang, X. H. Chen, C. L. Yao, X. Y. Jin, K.-L. Wang, W. C. Huang, T. Y. Huang, Y. P. Zhao, Y. X. Zhai, D. Meng, S. Tan, R. Z. Liu, Z.-K. Wang, C. H. Zhu, K. Zhu, M. C. Beard, Y. F. Yan and Y. Yang, *Science*, 2021, **371**, 636–640.
- 4 W. S. Yang, B.-W. Park, E. H. Jung, N. J. Jeon, Y. C. Kim, D. U. Lee, S. S. Shin, J. Seo, E. K. Kim, J. H. Noh and S. I. Seok, *Science*, 2017, **356**, 1376–1379.
- 5 Y. Zhao, F. Ma, Z. H. Qu, S. Q. Yu, T. Shen, H.-X. Deng, X. B. Chu, X. X. Peng, Y. B. Yuan, X. W. Zhang and J. B. You, *Science*, 2022, **377**, 531–534.
- 6 C. T. Zuo, H. J. Bolink, H. W. Han, J. S. Huang, D. Cahen and L. M. Ding, *Adv. Sci.*, 2016, **3**, 1500324.
- 7 <https://www.nrel.gov/pv/cell-efficiency.html>.
- 8 J. Jeong, M. Kim, J. Seo, H. Z. Lu, P. Ahlawat, A. Mishra, Y. G. Yang, M. A. Hope, F. T. Eickemeyer, M. Kim, Y. J. Yoon, I. W. Choi, B. P. Darwich, S. J. Choi, Y. Jo, J. H. Lee, B. Walker, S. M. Zakeeruddin, L. Emsley, U. Rothlisberger, A. Hagfeldt, D. S. Kim, M. Grätzel and J. Y. Kim, *Nature*, 2021, **592**, 381–385.
- 9 Z. Liang, Y. Zhang, H. F. Xu, W. J. Chen, B. Y. Liu, J. Y. Zhang, H. Zhang, Z. H. Wang, D.-H. Kang, J. R. Zeng, X. Y. Gao, Q. S. Wang, H. J. Hu, H. M. Zhou, X. B. Cai, X. Y. Tian, P. Reiss, B. M. Xu, T. Kirchartz, Z. G. Xiao, S. Y. Dai, N.-G. Park, J. J. Ye and X. Pan, *Nature*, 2023, **624**, 557–563.
- 10 J. Park, J. Kim, H.-S. Yun, M. J. Paik, E. Noh, H. J. Mun, M. G. Kim, T. J. Shin and S. I. Seok, *Nature*, 2023, **616**, 724–730.
- 11 H. N. Chen, *Adv. Funct. Mater.*, 2017, **27**, 1605654.
- 12 C. H. Chen, Y. H. Lou, K. L. Wang, Z. H. Su, C. Dong, J. Chen, Y. R. Shi, X. Y. Gao and Z. K. Wang, *Adv. Energy Mater.*, 2021, **11**, 2101538.
- 13 Y. S. Ge, H. B. Wang, C. Wang, C. Wang, H. L. Guan, W. L. Shao, T. Wang, W. J. Ke, C. Tao and G. J. Fang, *Adv. Mater.*, 2023, **35**, e2210186.
- 14 W. Hui, L. F. Chao, H. Lu, F. Xia, Q. Wei, Z. H. Su, T. T. Niu, L. Tao, B. Du, D. L. Li, Y. Wang, H. Dong, S. W. Zuo, B. X. Li, W. Shi, X. Q. Ran, P. Li, H. Zhang, Z. B. Wu, C. X. Ran, L. Song, G. C. Xing, X. Y. Gao, J. Zhang, Y. D. Xia, Y. H. Chen and W. Huang, *Science*, 2021, **371**, 1359–1364.
- 15 W. L. Shao, H. B. Wang, F. H. Ye, C. Wang, C. Wang, H. S. Cui, K. L. Dong, Y. S. Ge, T. Wang, W. J. Ke and G. J. Fang, *Energy Environ. Sci.*, 2023, **16**, 252–264.
- 16 Y. T. Du, Y. Wang, J. H. Wu, Q. Chen, C. Y. Deng, R. Ji, L. X. Sun, L. N. Tan, X. Chen, Y. M. Xie, Y. F. Huang, Y. Vaynzof, P. Gao, W. H. Sun and Z. Lan, *InfoMat*, 2023, **5**, e12431.
- 17 Y. Zhao, X. Zhang, X. F. Han, C. Y. Hou, H. Z. Wang, J. B. Qi, Y. G. Li and Q. H. Zhang, *Chem. Eng. J.*, 2021, **417**, 127912.
- 18 Q. Sun, S. C. Duan, G. Liu, X. X. Meng, D. Hu, J. G. Deng, B. Shen, B. N. Kang and S. R. P. Silva, *Adv. Energy Mater.*, 2023, **13**, 2301259.
- 19 F. Guo, W. X. He, S. D. Qiu, C. Wang, X. H. Liu, K. Forberich, C. J. Brabec and Y. H. Mai, *Adv. Funct. Mater.*, 2019, **29**, 1900964.
- 20 Y. Ma, Q. Z. Song, X. Y. Yang, H. C. Zai, G. Z. Yuan, W. T. Zhou, Y. H. Chen, F. T. Pei, J. Q. Kang, H. Wang, T. L. Song, X. Y. Wang, H. P. Zhou, Y. J. Li, Y. Bai and Q. Chen, *Nano Energy*, 2023, **108**, 108250.
- 21 J. H. Ren, T. H. Liu, B. C. He, G. B. Wu, H. Gu, B. Z. Wang, J. L. Li, Y. L. Mao, S. Chen and G. C. Xing, *Small*, 2022, **18**, 2203536.
- 22 C. X. Ran, W. Y. Gao, N. X. Li, Y. D. Xia, Q. Li, Z. X. Wu, H. P. Zhou, Y. H. Chen, M. Q. Wang and W. Huang, *ACS Energy Lett.*, 2018, **4**, 358–367.
- 23 A. Ummadisingu, L. Steier, J.-Y. Seo, T. Matsui, A. Abate, W. Tress and M. Grätzel, *Nature*, 2017, **545**, 208–212.
- 24 C. Luo, G. H. J. Zheng, F. Gao, X. J. Wang, Y. Zhao, X. Y. Gao and Q. Zhao, *Joule*, 2022, **6**, 240–257.
- 25 C. Zhu, C. Y. Wang, P. X. Zhang, S. Ma, Y. H. Chen, Y. Zhang, N. Yang, M. Q. Xiao, X. H. Cheng, Z. Y. Gao, K. C. Wen, X. X. Niu, T. L. Song, Z. H. Su, H. C. Zai, N. X. Li, Z. J. Huang, Y. Zhang, H. Wang, H. P. Zhou, F. Xiao, P. W. Chen, X. Y. Wang, J. W. Hong, J. P. Wang, Y. Bai, X. Y. Gao and Q. Chen, *Joule*, 2023, **7**, 2361–2375.
- 26 L. Chu, S. B. Zhai, W. Ahmad, J. Zhang, Y. Zang, W. S. Yan and Y. F. Li, *Nano Res. Energy*, 2022, **1**, 9120024.
- 27 Z. H. Xiong, L. K. Lan, Y. Y. Wang, C. X. Lu, S. C. Qin, S. S. Chen, L. Y. Zhou, C. Zhu, S. G. Li, L. Meng, K. Sun and Y. F. Li, *ACS Energy Lett.*, 2021, **6**, 3824–3830.
- 28 C. Q. Ma, M.-C. Kang, S.-H. Lee, S. J. Kwon, H.-W. Cha, C.-W. Yang and N.-G. Park, *Joule*, 2022, **6**, 2626–2643.
- 29 X. Zhao, Y. J. Qiu, M. Wang, D. X. Wu, X. P. Yue, H. L. Yan, B. B. Fan, S. X. Du, Y. Q. Yang, Y. Y. Yang, D. N. Li, P. Cui, H. Huang, Y. F. Li, N.-G. Park and M. C. Li, *ACS Energy Lett.*, 2024, 2659–2669.
- 30 X. Y. Liu, J. Min, Q. Chen, T. Liu, G. P. Qu, P. F. Xie, H. Xiao, J.-J. Liou, T. Park and Z. X. Xu, *Angew. Chem., Int. Ed.*, 2022, **61**, e202117303.
- 31 J. J. Yoo, G. Seo, M. R. Chua, T. G. Park, Y. L. Lu, F. Rotermond, Y.-K. Kim, C. S. Moon, N. J. Jeon, J.-P. Correa-Baena, V. Bulović, S. S. Shin, M. G. Bawendi and J. Seo, *Nature*, 2021, **590**, 587–593.
- 32 K. M. Deng, Q. H. Chen and L. Li, *Adv. Funct. Mater.*, 2020, **30**, 2004209.
- 33 F. H. Isikgor, S. Zhumagali, L. V. T. Merino, M. De Bastiani, I. McCulloch and S. De Wolf, *Nat. Rev. Mater.*, 2022, **8**, 89–108.
- 34 H. D. Guo, W. C. Xiang, Y. Y. Fang, J. R. Li and Y. Lin, *Angew. Chem., Int. Ed.*, 2023, **62**, e202304568.
- 35 L. P. Wang, J. X. Xia, Z. Yan, P. Q. Song, C. Zhen, X. Jiang, G. Shao, Z. L. Qiu, Z. H. Wei, J. H. Qiu and M. K. Nazeeruddin, *Adv. Funct. Mater.*, 2022, **32**, 2204725.
- 36 Y. Q. Wang, Y. Wu, M. Z. Li, Z. Z. Wang, W. Z. Zhang, C. W. Shi and P. Cui, *ChemistrySelect*, 2023, **8**, e202303395.
- 37 L. Krückemeier, B. Krogmeier, Z. F. Liu, U. Rau and T. Kirchartz, *Adv. Energy Mater.*, 2021, **11**, 2003489.
- 38 S. Hassan Kareem, M. Harjan Elewi, A. Muhson Naji, D. S. Ahmed and M. K. A. Mohammed, *Chem. Eng. J.*, 2022, **443**, 136469.